Synthesis and *in vitro* cellular interactions of superparamagnetic iron nanoparticles with a crystalline gold shell

Sulalit Bandyopadhyay[*], *Gurvinder Singh*[1], *Ioanna Sandvig*[2], *Axel Sandvig*[2,3], *Roland Mathieu*[4], *P. Anil Kumar*[4], *Wilhelm Robert Glomm*[1,5]

[1]Ugelstad Laboratory, Department of Chemical Engineering,

[2] MI Lab and Department of Circulation and Medical Imaging,

Norwegian University of Science and Technology (NTNU), N-7491 Trondheim, Norway.

[3] Department of Neurosurgery, Umeå University Hospital, Umeå, Sweden.

[4]Department of Engineering Sciences, Uppsala University, Box 534, SE-75121 Uppsala, Sweden.

[5]Sector for Biotechnology and Nanomedicine, SINTEF Materials and Chemistry, N-7465 Trondheim, Norway.

[*]Corresponding author's email address: sulalit.bandyopadhyay@ntnu.no

ABSTRACT

Fe@Au core-shell nanoparticles (NPs) exhibit multiple functionalities enabling their effective use in applications such as medical imaging and drug delivery. In this work, a novel synthetic method was developed and optimized for the synthesis of highly stable, monodisperse Fe@Au NPs of average diameter ~24nm exhibiting magneto-plasmonic characteristics. Fe@Au NPs were characterized by a wide range of experimental techniques, including Scanning (Transmission) Electron Microscopy (S(T)EM), X-Ray Diffraction (XRD), X-Ray Photoelectron Spectroscopy (XPS), Energy Dispersive X-Ray Spectroscopy (EDX), Dynamic Light Scattering (DLS) and UV-Vis spectroscopy. The formed particles comprise an amorphous iron core with a crystalline Au shell of tunable thickness, and retain the superparamagnetic properties at room temperature after formation of a crystalline Au shell. After surface modification, PEGylated Fe@Au NPs were used for *in vitro* studies on olfactory ensheathing cells (OECs) and human neural stem cells (hNSCs). No adverse effects of the Fe@Au particles were observed post-labelling, both cell types retaining normal morphology, viability, proliferation, and motility. It can be concluded that no appreciable toxic effects on both cell types, coupled with multifunctionality and chemical stability make them ideal candidates for therapeutic as well as diagnostic applications.

Keywords: Core-shell nanoparticles, oleylamine, multifunctional, contrast agents, cytotoxicity, multimodal imaging, cell labelling

1.1 Introduction

Synthesis of magnetic nanoparticles (MNPs) of tunable sizes has received a great scientific attention owing to their applications in targeted drug delivery, magnetic resonance imaging (MRI) and treatment of cancer by hyperthermia.[1-8] A common property exploited in life sciences and biomedicine is superparamagnetism allowing the alignment of all spins under an external magnetic field.[9] Despite their tremendous use in biomedical applications, MNPs often tend to aggregate due to strong interparticle dipolar interactions in high ionic strength environment of biological solutions.[10] This causes the enlargement of nanoparticle size, influencing their magnetic properties and limiting their practical use. While MNPs with higher magnetic moment and higher anisotropy would be ideal to improve their performance and dosage, they are often hampered by a low degree of chemical stability, increased toxicity coupled with low plasma half life.[11] Therefore, a major challenge is to increase solution stability and reduce NP toxicity without compromising their magnetic properties.

To overcome these limitations, several procedures have been reported whereby the MNPs are modified with a thin layer of polymers/organic molecules, metal oxide or a metal.[12-14] Among these, a thin protective shell of gold (Au) around the MNPs provides high stability due to its chemical inertness, low cytotoxicity, simple bioconjugation through well-understood surface chemistry such as Au-S,[15] and high catalytic activity while supported on metal or metal oxide supports.[16] Upon further functionalization with molecules such as PEG (Poly (ethylene glycol)), NP aggregation can also be prevented, besides exploiting cloaking properties of PEG.[17] Au NPs display tunable and environmentally sensitive localized surface plasmon resonance (LSPR) within the visible range, which makes them suitable candidates for biosensors, and good contrast agents for computed tomography (CT)[18, 19] as well as photo-acoustic

imaging.[20] Thus, core@shell NPs formed by unifying a nanoscale magnetic core within a thin metallic shell can act as a dual contrast agent for MRI and CT. To date, various approaches have been developed for the synthesis of MNPs@Au, such as hydroxyl amine seeding, reverse micelle templating, attachment of Au NPs onto amino-silane modified iron oxide NPs, laser ablation, sonochemical reaction, γ-ray radiation, etc . [8, 21-24]

Despite a small number of successful approaches for the synthesis of MNPs@Au and the exploration of their applications in different areas, many issues related to the precise control of Au shell thickness, and the detailed characterization of resultant MNPs@Au need to be addressed. In addition, some limitations associated with earlier methods also include time-consuming purification steps, intricate sequence of chemical reactions, broad size distribution, and poor magnetic responses due to uncontrolled or uneven coating of Au shell around MNPs. [25] The control over size of the resultant MNPs@Au is very important which not only has a pronounced effect on toxicity and retention but also on mode of administration. In some cases, successive gold coating steps are needed to ensure sufficiently stable Fe@Au NPs.[26] Remaining solvents or surfactants may also result in opsonization *in vivo* and other potential side effects, and thus biocompatibility becomes a serious concern.[27]

Here, we report a new synthetic procedure for the formation of Fe@Au NPs with a crystalline Au shell on amorphous Fe NPs, their solution and magnetic properties, as well as their interaction with two cell lines. Our approach provides control over Au shell thickness via tuning the concentration of Au salt in the solution. First, Fe NPs were produced via thermal decomposition of iron pentacarbonyl ($Fe(CO)_5$) in the presence of oleylamine (OAm).[28] Later, these NPs were transferred to an aqueous phase, and a shell of Au was grown over presynthesized Fe NPs seeds via reduction of Au salt in the presence of sodium citrate. Scanning

(Transmission) electron microscopy (S(T)EM), X-ray diffraction (XRD), X-ray photoelectron spectroscopy (XPS), energy Dispersive X-Ray Spectroscopy (EDX), dynamic light scatterning (DLS), and ultraviolet-visible spectroscopy (UV-Vis) were used to characterize the Fe@Au NPs. These NPs were subsequently functionalized with O-[2-(3-Mercaptopropionylamino)ethyl]-O′-methylpolyethylene glycol (PEG-SH) molecules which have been used at various concentrations for *in vitro* labeling of two different cell types which are promising candidates for regenerative therapy of the central nervous system:[29, 30] olfactory ensheathing cells (OECs) and human neural stem cells (hNSCs). These two cell types differed in terms of uptake and localization of the Fe@Au NPs post-labelling, while no cytotoxic effects were observed irrespective of label concentration or length of co-incubation with the NPs. The magnetic properties of Fe, Fe@Au, and PEGylated Fe@Au NPs were measured by Quantum Design MPMS system indicating supermagnetic behavior.Thus, Fe@Au NPs were found to be have low cytotoxicity, aptly suited for a wide array of applications including bioimaging, drug delivery and other biodiagnostic and/or biomedical applications.

1.2 Materials and Methods

Iron pentacarbonyl ($Fe(CO)_5$, 99.99%), octadecene (ODE, 90%), oleylamine (OAm, 70%), chloroauric acid (99.999%), sodium citrate, O-[2-(3-Mercaptopropionylamino)ethyl]-O′-methylpolyethylene glycol (PEG-SH) of molecular weight 5000 Da were purchased from Sigma Aldrich.

1.2.1 Synthesis of Fe NPs

Fe NPs were synthesized via thermal decomposition of $Fe(CO)_5$ in ODE in the presence of OAm. The reaction scheme modified from the one reported by Sun *et al* [31] is detailed herein. In essence, a mixture of ODE (50 mL) and OAm (740 µL) was degassed under Ar atmosphere and vigorous stirring at 120^0C for 30 min. The temperature was raised to 180^0C and 1.8 mL of

$Fe(CO)_5$ was injected into the hot reaction mixture and the reaction was continued for 20 min. After cooling down to room temperature, the supernatant was decanted and the magnetic bar coated with Fe NPs was washed with 20 mL hexane and 40 mL acetone. Fe NPs were magnetically separated, and the product was washed two times with 20 mL acetone. Subsequently, these Fe NPs were dried in a stream of nitrogen.

1.2.2 Synthesis of Fe@Au NPs

The schematic protocol for Fe@Au NPs synthesis is illustrated in Figure 1. 5 mg of the as synthesized Fe NPs were dissolved in 10 mL of 10 mM sodium citrate solution using sonication at 80^0C for half an hour. Citrate stabilized Fe seed solution (brown solution) was added to a 50 ml reaction flask and the resultant solution was maintained to 70^0C under mild stirring. 10 mL of 1.5 mM Chloroauric acid (the concentration of the gold precursor was optimized by performing experiments at concentrations both below and above this experimental value) was added dropwise and allowed to react for 20 min under vigorous stirring. The solution turned purplish red around 8 minutes after reaction. Thereafter, the solution was cooled down to room temperature, and Fe@Au NPs were magnetically separated to remove free Au NPs. A video of the synthesis protocol showing the colour change during the course of the reaction and influence of the magnet on the final product can be found in the supporting information.

1.2.3 PEG Coating of Fe@Au NPs

2 mg of PEG-SH was mixed with 5 mg of the as synthesized Fe@Au NPs dissolved in 5 mL of MQ water and stirred for 1 hour to covalently modify the surface of the NPs.[32] The resulting PEG coated Fe@Au NPs were collected by centrifugation at 10000rpm for 20 mins and washed twice with MQ water. These NPs were stored at concentrations of 1 mg/mL at 4°C to prevent further aggregation.

1.2.4 Cell studies

Two different cell types were used for the cell studies, namely OECs and hNSCs. OECs were purified from neonatal Fischer rats at P8 according to Barnett and Roskams.[33] Purified OECs were cultured in Dulbecco's Modified Eagle's Medium (DMEM GlutaMAX) with 1.25% gentamicin and 5% FBS (Autogen Bioclear) on poly-L-lysine- (PLL) coated multi-well plates (Corning). The cultures were supplemented with 500ng/ml fibroblast growth factor 2 (FGF2) (Peprotech, London, UK), 50ng/ml heregulin (hrgβ1) (R&D Systems Europe Ltd, Abingdon, UK), and 10^{-6} M forskolin.

Undifferentiated H9-derived, hNSCs (Gibco, Invitrogen) were cultured on laminin-coated multi-well plates (Corning) in StemPro NSC serum-free medium (Gibco, Invitrogen) containing 20ng/ml basic recombinant human fibroblast growth factor (bFGF) (Gibco, Invitrogen) and 20ng/ml recombinant human epidermal growth factor (EGF) (Gibco, Invitrogen).

1.2.4.1 Cell labelling with Fe@Au NPs

PEG coated Fe@Au NPs were added to 50% confluent OEC and hNSC cultures at concentrations of nanoparticles/media volume of 1 μg/mL, 100μg/mL, 1mg/ml and incubated for 6h, 12h, and 24h at 37°C with 7% CO_2 and 5% CO_2, respectively.

1.2.4.2 LIVE/DEAD® cell viability assay

The viability of OECs and hNSCs was qualitatively assessed by visualization of live and dead cells, stained by calcein and ethidium homodimer-1 (EthD-1), respectively, using LIVE/DEAD® assay (Invitrogen, Life Technologies) immediately after 6h, 12h and 24h incubation with Fe@Au-PEG NPs. LIVE/DEAD® solution was prepared in 4.5 mL sterile PBS with 2.7 μL calcein (Invitrogen), and 12 μL ethidium homodimer (Invitrogen), added to the labeled cell cultures at 1:1 (v/v), and incubated for 30 min at 37°C. The cultures were subsequently imaged

on an Axiovert 200M fluorescent microscope (Zeiss, Germany) using AxioVision Rel. 4.3 software.

1.2.4.3 Prussian Blue staining

Prussian Blue kit was used for detection of intracellular iron. Following 12h of incubation with PEG coated Fe@Au NPs, OECs and hNSCs were fixed with 4% paraformaldehyde and subsequently stained with Prussian Blue according to the supplier's recommended protocol.

1.2.5 Characterization Techniques

1.2.5.1 Scanning (Transmission) Electron Microscopy [S(T)EM] and Energy Dispersive X-Ray Spectroscopy [EDX]

S(T)EM images and EDX analyses were acquired using a Hitachi S-5500 electron microscope operating at 30kV accelerating voltage. TEM images were obtained in bright field mode. TEM grids were prepared by placing several drops of the solution on a Formvar carbon coated copper grid (Electron Microscopy Sciences) and wiping immediately with Kimberly-Clark kimwipes to prevent further aggregation owing to evaporation at room temperature.

1.2.5.2 Dynamic Light Scattering [DLS]and Zeta Potential Measurement

The size distribution and zeta potential of the NPs were were measured using a Malvern Zetasizer Nano-ZS instrument, and the manufacturer's own software. The solvent used for the Fe NPs was n-Hexane while for the other NPs, MQ water was used.

1.2.5.3 Ultraviolet-Visible Spectroscopy [UV-Vis]

UV-Vis spectra were acquired with a UV-2401PC (Shimadzu) spectrophotometer. The spectra were collected over the spectral range from 200-800 nm.

1.2.5.4 Xray Photoelectron Spectroscopy (XPS)

XPS analyses were performed using a Kratos Axis Ultra DLD spectrometer (Kratos Analytical, UK), equipped with a monochromatized aluminum X-ray source (Al, hυ = 1486.6 eV) operating at 10 mA and 15 kV (150 W). A hybrid lens (electrostatic and magnetic) mode was employed

along with an analysis area of approximately 300 µm X 700 µm. Survey spectra were collected over the range of 0-1100 eV binding energy with analyzer pass energy of 160 eV, and high resolution spectra of C 1s, O 1s, Fe 2p and Au 4f were obtained with an analyzer pass energy of 20 eV. XPS data were processed with Casa XPS software (Casa Software Ltd., UK).

1.2.5.5 X-Ray Diffraction (XRD)

XRD patterns were collected from Bruker AXS D8Focus with Cu K_α radiation (λ=1.5418 Å). Samples for XRD measurement were prepared by depositing several drops of concentrated solution of NPs on a single crystalline silicon holder.

1.2.5.6 Magnetic Measurements

Zero-field-cooled (ZFC) and field-cooled (FC) magnetization versus temperature (M-T) and room temperature magnetization versus field (M-H) measurements were performed using a Quantum Design MPMS system.

1.3 Results and Discussion

The main steps involved in a typical synthesis of Fe@Au NPs and subsequent surface modification with PEG are shown in Figure 1. Fe NPs were synthesized using a previously reported method.[31] These Fe NPs rapidly oxidize upon exposure to the air, forming a thin surface layer of natural iron oxide. The S(T)EM image displayed in Figure 2(a) and its inset reveal a core-shell morphology of Fe MNPs, *i.e.*, Fe@Fe_xO_y. It is difficult to predict the exact nature of the shell composition as both the core and shell are amorphous in nature as confirmed by XRD measurements, which is also consistent with previous reports (Figure 2(e)).[34, 35] The number average diameter of these NPs was measured over 200 NPs and was found to be 14 ± 1 nm. The Fe NPs were dried after removal of the surfactant by washing with hexane and acetone several times, and transferred into an aqueous phase in the presence of sodium citrate. The

citrate-functionalized Fe NPs were found to be stable in an aqueous phase without any aggregation (Figure S1 in the supporting information). Later, a thin coating of Au was carried out in aqueous medium using water soluble Fe NPs as heterogeneous nucleation sites, leading to the formation of a continuous shell of Au around the Fe NPs.The resultant product of Fe@Au NPs were magnetically separated to remove freely suspended Au NPs, and redispersed in an aqueous phase.

Representative bright field (BF) S(T)EM images shown in figure 2(b) exhibit an increment in an average diameter ~24± 5 nm of Fe@Au NPs which are subsequently functionalized with PEG-SH (Figure 2(c)). From these data, the thickness of the Au shell is calculated to be ~ 5 nm. DLS measurements, however, show larger sizes of 34 ± 4 nm (Fe NPs), 71 ± 4 nm (Fe@Au NPs) and 72 ± 5 nm (PEG Fe@Au NPs), respectively, in comparison to analysis via S(T)EM. The reason for this discrepancy can be attributed either due to DLS measuring the hydrodynamic rather than the core radius of the NPs as measured by S(T)EM, a weak interparticle dipolar interaction among NPs causing weak interparticle coupling, or a combination. It is difficult to visualize a core-shell morphology of as-prepared Fe@Au NPs in electron microscopy because Au has a higher atomic number than Fe, contributing to high contrast while imaging. A shell of Au coating around Fe NPs can be confirmed by EDX elemental analysis, indicating the presence of Fe and Au in NPs (inset in Figure 2(b)). Moreover, UV-vis spectroscopy was used to characterize the various steps of Fe NP surface functionalization (Figure 2 (d)). It can be noted from the UV-Vis spectra that Fe NPs do not show a prominent absorption peak in the visible, whereas Fe@Au NPs display an absorption peak at ~ 525 nm, which is a characteristic LSPRof Au NPs. We observe a red shift in the absorbance peak (~528 nm) for PEG coated Fe@Au NPs.

The bathochromic shift is an indication of the increase in the size of the NPs following PEG-coating, as predicted by Mie-Drude theory. [36]

XRD pattern of the Fe@Au NPs shows diffraction peaks at 2Θ values of 38.3, 44.4, 64.7, 77.7, corresponding to (111), (200), (220), (311) planes, respectively, revealing the crystalline nature of the Au shell on amorphous Fe NPs [34, 37](Figure 2 (e)). We also estimated the average crystallite size of Fe@Au NPs obtained from half width diffraction peaks using Scherrer`s formula, yielding ~8.5± 2 nm, which is very small compared to the size (~24± 5 nm) measured by TEM. This can be understood by considering the all diffraction peaks in XRD pattern corresponding to only crystalline phase of the materials (i.e., the Au layer), and an average size measured by XRD corresponds to the actual size of the Au shell. Such a shell thickness of Au layer ~4± 1 nm from XRD is in good agreement with shell thickness as measured by S(T)EM. XPS studies were also conducted in order to examine the Au coating on Fe NPs, revealing the presence of Fe 2p before and both Fe 2p and Au 4f after Au coating (Figure 3(a,c)). In addition, a high resolution XPS spectrum of Fe NPs shows three photoelectron peaks at ~711 eV and ~725 eV corresponding to binding energies of $2p_{3/2}$ and $2p_{1/2}$ of oxidized Fe (III), and ~707 eV assigned to zero-valent Fe (Fig. 3(b)).[38] Figure 3(d) shows a high resolution spectrum of Au4f which consists of two peaks with binding energies of ~84 eV and ~87 eV corresponding to elemental Au(0), further confirming the presence of Au coating over Fe NPs. Taken together, our results from S(T)EM, DLS, EDX XRD, and XPS provide evidence for the successful coating of the Fe NPs with a crystalline Au layer.

Zeta potential measurements of the Fe@Au and Fe@Au-PEG NPs showed zeta potential values of -49.4 mV and -36.2 mV respectively. These high values essentially account for the electrosteric stability of the particles in aqueous solution, possibly enabling prolonged circulation times for *in vivo* applications. Furthermore, the effect of Au precursor concentration on the formation of Fe@Au NPs was investigated for controlling the surface deposition of Au onto Fe NPs. At low concentration of Au^{+3} precursor (0.9 mM), we noticed a low yield of Fe@Au NPs, where the majority of Fe NPs remained unmodified following Au coating (Figure 4(a)). When the concentration was raised to 3.4 mM, elongated Fe@Au NPs with high yield were obtained (Figure 4(b)). The size of these NPs was found to be ~28±5 nm which is larger than the reference Fe@Au NPs (~24± 5 nm) synthesized at Au concentration 1.5 mM, leading to increase in the shell thickness from ~5 nm to ~7 nm based on S(T)EM size distribution analysis. Similary, a crystallite size analysis from the XRD patterns reveal an increase in shell thickness from ~4±1 nm to ~6±2 nm following an increment from 1.5 mM to 3.4 mM of Au^{+3} precursor, which is consistent with STEM results (Figure S2 in the supporting information). A bathochromic shift in UV-Vis spectra is observed from 528 nm to 535 nm with increasing gold precursor concentration, indicating thicker gold coating (Figure 4(c)). In addition, an evolution of a second LSPR band above 600 nm with increasing gold precursor concentration is observed, which can be attributed to a change in the nanoparticle shape after gold coating.

Figure 5(a) shows the zero- field- cooled (ZFC) and field cooled (FC) magnetization versus temperature curves recorded in a weak magnetic field (H = 20 Oe) for Fe and Fe@Au NPs. Both samples show ZFC magnetization curves reminiscent of superparamagnets.When the sample is cooled under zero field, it shows no net alignment of spins at low temperature, resulting in a very

low magnetization. As the temperature increases, the spins become progressively “unblocked”, aligning toward the applied field direction, and the magnetization increases until it reaches a maximum value at a temperature commonly referred as the mean blocking temperature (T_b) of the sample. At temperature above T_b (about 90 K in our samples) the thermal energy (k_BT) overcomes the magnetic anisotropy energy barrier (i.e., increased dynamic rotation of the spins prevents the alignment in the field direction), and magnetization starts decreasing with further increase in temperature [9].

However, the nature of FC magnetization curves of Fe and Fe@Au NPs are significantly different. The magnetization-temperature (M-T) curves of the Fe NPs are reminiscent of a strongly interacting nanoparticle system, with the FC magnetization value decreasing below the T_b on cooling down and the ZFC magnetization starting to rise only as T_b is approached on warming up.[39] In contrast, the Fe@Au NPs display M-T curves that are reminiscent of a weakly interacting nanoparticle system; the FC magnetization does not decrease below T_b and the ZFC magnetization starts to rise right from the lowest measured temperature. This observation matches very well with the prediction that the coating of (5 nm thick) Au shell coupled with citrate stabilization helps in separating the Fe moments and hence reduces the interaction between them.

Figure 5(b) shows the magnetization versus the magnetic field at 300K obtained by cycling the field between -30kOe and 30kOe. A negligible coercivity and remanence in the hysteresis loops indicates the super-paramagnetic nature of the NPs. The M-H curves become rounder or S-shaped like as Au is coated on the NPs, again reflecting the weakening of interparticle

interaction. It can be seen that the saturation magnetizations of the NPs are lower than that reported for bulk phase at room temperature (~218 emu/g).[40] It is well established that that the saturation magnetization of nanomaterials decreases (in comparison to the bulk) with decreasing particle size owing to existence of surface spin disorder or the magnetic dead layer.[41] Here it is important to note that the magnetization value in emu/g for the Fe@Au NPs does not represent the actual magnetic moment of the Fe core, but it is underestimated because of the weight of Au that contributes to the total mass of the sample that is used for the magnetic measurements. In fact, if this discrepancy is corrected by roughly subtracting the weight of Au (calculated from the volume ratio of Fe and Au in a Fe@Au NP) enhanced values for the Fe magnetization are obtained. This enhancement can be explained by the fact that the coating of Au shell reduces the magnetic dead layer in our samples. Further, in the present case the possibility of increased crystallinity of Fe core on addition of Au shell cannot be ruled out, which also can lead to increased magnetic moment. This enhancement in the magnetization value of the NPs on Au addition is another advantage for biomagnetic applications. For example, higher magnetization increases the MRI contrast with the applied magnetic field due to the stronger interferences with the relaxation times of water which is the principal proton source in MRI signal.[42] Additionally, for applications that require particle manipulation by an external magnetic field at a distance, it is essential that the particle saturation magnetization is as high as possible.[43] Our magnetic measurements on the Fe@Au-PEG sample (Figure S3 in the supporting information) prove that the addition of PEG molecules further weakens the magnetic interaction between the Fe moments. Having characterized the Fe@Au NPs, PEGylated NPs were used to study their interactions wth two different cell types.

In order to assess the impact of the synthesized MNPs on cell lines, Live/dead® assays were performed at different time points after introduction of the Fe@Au-PEG NPs to cell cultures of OECs and hNSCs, respectively. Co-incubation at 37°C did not reveal observable toxic effects of the NPs on either OECs or hNSCs. Both cell types retained viability as well as normal morphology and motility compared to controls [Fig. 6(a),(b),(d),(e)]. Moreover, cell proliferation in terms of expected confluence at 24h intervals did not seem to be altered by the presence of the NPs in the cultures. The above findings were consistent in all samples and were independent of NP concentration used for co-incubation.

Differential interference contrast (DIC) images and Prussian Blue assay results indicate uptake of Fe@Au –PEG NPs in >90% of both OECs and hNSCs [Fig. 6(c),(f)]. A tendency for peri-membrane localization of the Fe@Au NPs, rather than intracellular localization, was observed in the OECs. Consistent with the above, these observations were independent of length of co-incubation or NP concentration used, while it appeared that the two cell types displayed different affinity towards the NPs. Quantification of potential peri-membrane/intracellular NP concentration was beyond the scope of the present study. Evaluation of NP-induced toxicity *in vitro* is important before proceeding to *in vivo* applications as it eliminates the risk of unwanted effects of the NPs on the cell of interest. At the same time, potential cytotoxic effects of the NPs as well as cellular uptake will be contingent on cell type and *in vitro* labeling protocol.[44] In this study, the Fe@Au NPs were applied to cells with very different antigenic, metabolic and functional profiles, i.e. a glial cell (OEC) and a stem cell (hNSC), both of which are highly relevant in tissue engineering and image-guided therapy following central nervous system (CNS) injury.[45, 46] The lack of observable toxic effects of the Fe@Au NPs on either cell type is very

promising with regard to future *in vivo* application involving the specific cells. On the other hand, the differential affinity of the OECs and hNSCs to the particles suggests that labeling and imaging protocols for *in vivo* application must be optimized for the individual cell types, consistent with previous findings. [44]

1.4 Conclusion

In summary, we have optimized and developed the synthetic conditions for designing multifunctional core-shell type NPs consisting of magnetic core surrounded by a uniform, crystalline shell of Au. The thickness of gold shell can be tuned by varying Au precursor concentration. This approach can further be extended to the coating of other noble metals with controllable thickness where metallic shell provides a surface for easy chemical functionalization and long-term stabilization of the magnetic core under physiological conditions. S(T)EM, EDX , DLS, UV-Vis and XRD techniques were used to confirm the uniform coating of Au shell around an Fe core. As-synthesized Fe NPs with core-shell morphology were confirmed by XPS results which indicates that an inner core and an outer shell of MNPs are formed by Fe^0 and oxidized Fe, respectively. The presence of Au peaks in survey and high resolution XPS spectra affirm the Au coating around the magnetic core, which is also evident from XRD measurements indicating an amorphous state of Fe NPs prior to Au coating. After Au coating on Fe NPs, a crystalline phase arises which is attributed to the Au shell. The magnetic properties of NPs at various steps of surface modification were characterized, and we observe a superparamagnetic behavior at room temperature due to the absence of hysteresis loop in M-H curves at 300 K, and T_b<300 K. From these results, it is clear that MNPs retain substantial magnetic properties even after Au coating. In addition, it has been shown that PEGylated Fe@Au NPs have no observable cytotoxic effects on either OECs or NSCs, with a tendency of peri-membrane internalization, to

be further understood through *in vitro* studies. The lack of observable toxic effects of the Fe@Au NPs on either cell type is very promising with regard to future *in vivo* application involving the specific cells. Magneto-plasmonic properties exhibited by these hybrid NPs enable them suitable for theranostic as well as multimodal imaging uses.

1.5 Acknowledgement

The authors would like to thank Liaison Committee between the Central Norway Regional Health Authority (RHA) and NTNU, NorFab for financial support in connection to use of NTNU Nanolab, Swedish Research Council (VR) and the the Swedish Foundation for International Cooperation in Research and Higher Education (STINT) for the financial support.

1.6 References

[1] S. Laurent, D. Forge, M. Port, A. Roch, C. Robic, L.V. Elst, R.N. Muller,Magnetic Iron Oxide Nanoparticles: Synthesis, Stabilization, Vectorization, Physicochemical Characterizations, and Biological Applications (vol 108, pg 2064, 2008), Chem Rev, 110 (2010) 2574-2574.

[2] M.A. Abakumov, S.A. Shein, H. Vishvasrao, N.V. Nukolova, M. Sokol'ski-Papkov, T.O. Sandalova, I.L. Gubskii, N.F. Grinenko, A.V. Kabanov, V.P. Chekhonin,Visualization of Experimental Glioma C6 by MRI with Magnetic Nanoparticles Conjugated with Monoclonal Antibodies to Vascular Endothelial Growth Factor, B Exp Biol Med+, 154 (2012) 274-277.

[3] A. Antonelli, C. Sfara, E. Manuali, I.J. Bruce, M. Magnani,Encapsulation of superparamagnetic nanoparticles into red blood cells as new carriers of MRI contrast agents, Nanomedicine-Uk, 6 (2011) 211-223.

[4] N. Arsalani, H. Fattahi, M. Nazarpoor,Synthesis and characterization of PVP-functionalized superparamagnetic Fe3O4 nanoparticles as an MRI contrast agent, Express Polym Lett, 4 (2010) 329-338.

[5] C.Y. Haw, F. Mohamed, C.H. Chia, S. Radiman, S. Zakaria, N.M. Huang, H.N. Lim,Hydrothermal synthesis of magnetite nanoparticles as MRI contrast agents, Ceram Int, 36 (2010) 1417-1422.

[6] E.K. Lim, Y.M. Huh, J. Yang, K. Lee, J.S. Suh, S. Haam,pH-Triggered Drug-Releasing Magnetic Nanoparticles for Cancer Therapy Guided by Molecular Imaging by MRI, Adv Mater, 23 (2011) 2436-+.

[7] C.R. Thomas, D.P. Ferris, J.H. Lee, E. Choi, M.H. Cho, E.S. Kim, J.F. Stoddart, J.S. Shin, J. Cheon, J.I. Zink,Noninvasive Remote-Controlled Release of Drug Molecules in Vitro Using Magnetic Actuation of Mechanized Nanoparticles, J Am Chem Soc, 132 (2010) 10623-10625.

[8] Z. Fan, M. Shelton, A.K. Singh, D. Senapati, S.A. Khan, P.C. Ray,Multifunctional Plasmonic Shell-Magnetic Core Nanoparticles for Targeted Diagnostics, Isolation, and Photothermal Destruction of Tumor Cells, Acs Nano, 6 (2012) 1065-1073.

[9] R. Krahne, G. Morello, A. Figuerola, C. George, S. Deka, L. Manna,Physical properties of elongated inorganic nanoparticles, Phys Rep, 501 (2011) 75-221.

[10] C. Sun, J.S.H. Lee, M.Q. Zhang,Magnetic nanoparticles in MR imaging and drug delivery, Adv Drug Deliver Rev, 60 (2008) 1252-1265.

[11] C.C. Berry, A.S.G. Curtis,Functionalisation of magnetic nanoparticles for applications in biomedicine, J Phys D Appl Phys, 36 (2003) R198-R206.

[12] S. Seino, T. Kinoshita, Y. Otome, T. Nakagawa, K. Okitsu, Y. Mizukoshi, T. Nakayama, T. Sekino, K. Niihara, T.A. Yamamoto,Gamma-ray synthesis of magnetic nanocarrier composed of gold and magnetic iron oxide, J Magn Magn Mater, 293 (2005) 144-150.

[13] L. Wang, J. Luo, M.J. Schadt, C.J. Zhong,Thin film assemblies of molecularly-linked metal nanoparticles and multifunctional properties, Langmuir, 26 (2010) 618-632.

[14] S.I. Stoeva, F.W. Huo, J.S. Lee, C.A. Mirkin,Three-layer composite magnetic nanoparticle probes for DNA, J Am Chem Soc, 127 (2005) 15362-15363.

[15] M. Famulok, J.S. Hartig, G. Mayer,Functional aptamers and aptazymes in biotechnology, diagnostics, and therapy, Chem Rev, 107 (2007) 3715-3743.

[16] R.A. Sperling, W.J. Parak,Surface modification, functionalization and bioconjugation of colloidal inorganic nanoparticles, Ther Innov Regul Sci, 47 (2013) 1333-1383.

[17] H. Otsuka, Y. Nagasaki, K. Kataoka,PEGylated nanoparticles for biological and pharmaceutical applications, Adv Drug Deliver Rev, 64 (2012) 246-255.

[18] D. Kim, S. Park, J.H. Lee, Y.Y. Jeong, S. Jon,Antibiofouling polymer-coated gold nanoparticles as a contrast agent for in vivo x-ray computed tomography imaging, Nanomed-Nanotechnol, 3 (2007) 352-352.

[19] H. Liu, Y.H. Xu, S.H. Wen, Q. Chen, L.F. Zheng, M.W. Shen, J.L. Zhao, G.X. Zhang, X.Y. Shi,Targeted Tumor Computed Tomography Imaging Using Low-Generation Dendrimer-Stabilized Gold Nanoparticles, Chem-Eur J, 19 (2013) 6409-6416.

[20] N. Khlebtsov, L. Dykman,Biodistribution and toxicity of engineered gold nanoparticles: a review of in vitro and in vivo studies, Chem Soc Rev, 40 (2011) 1647-1671.

[21] T. Zhou, B.Y. Wu, D. Xing,Bio-modified Fe3O4 core/Au shell nanoparticles for targeting and multimodal imaging of cancer cells, J Mater Chem, 22 (2012) 470-477.

[22] T. Jafari, A. Simchi, N. Khakpash,Synthesis and cytotoxicity assessment of superparamagnetic iron-gold core-shell nanoparticles coated with polyglycerol, J Colloid Interf Sci, 345 (2010) 64-71.

[23] J. Lin, W.L. Zhou, A. Kumbhar, J. Wiemann, J.Y. Fang, E.E. Carpenter, C.J. O'Connor,Gold-coated iron (Fe@Au) nanoparticles: Synthesis, characterization, and magnetic field-induced self-assembly, Journal of Solid State Chemistry, 159 (2001) 26-31.

[24] C.S. Levin, C. Hofmann, T.A. Ali, A.T. Kelly, E. Morosan, P. Nordlander, K.H. Whitmire, N.J. Halas,Magnetic-Plasmonic Core-Shell Nanoparticles, Acs Nano, 3 (2009) 1379-1388.

[25] J. Schotter, O. Bethge, T. Maier, H. Brueck,Recognition of biomolecular interactions by plasmon resonance shifts in single- and multicomponent magnetic nanoparticles, Appl Phys Lett, 93 (2008).

[26] J.L. Lyon, D.A. Fleming, M.B. Stone, P. Schiffer, M.E. Williams,Synthesis of Fe oxide core/Au shell nanoparticles by iterative hydroxylamine seeding, Nano Lett, 4 (2004) 719-723.

[27] C.R. Sun, K. Du, C. Fang, N. Bhattarai, O. Veiseh, F. Kievit, Z. Stephen, D.H. Lee, R.G. Ellenbogen, B. Ratner, M.Q. Zhang,PEG-Mediated Synthesis of Highly Dispersive Multifunctional Superparamagnetic Nanoparticles: Their Physicochemical Properties and Function In Vivo, Acs Nano, 4 (2010) 2402-2410.

[28] Z. Xu, Hou, Y., Sun, S.,Magnetic core/shell Fe3O4/Au and Fe3O 4/Au/Ag nanoparticles with tunable plasmonic properties, J Am Chem Soc, 129 (2007) 8698-8699

[29] S.C. Barnett, J.S. Riddell,Olfactory ensheathing cells (OECs) and the treatment of CNS injury: advantages and possible caveats, J Anat, 204 (2004) 57-67.

[30] M. Dihne, H.P. Hartung, R.J. Seitz,Restoring Neuronal Function After Stroke by Cell Replacement Anatomic and Functional Considerations, Stroke, 42 (2011) 2342-2350.

[31] Z.C. Xu, Y.L. Hou, S.H. Sun,Magnetic core/shell Fe3O4/Au and Fe3O4/Au/Ag nanoparticles with tunable plasmonic properties, J Am Chem Soc, 129 (2007) 8698-+.

[32] D. Kim, S. Park, J.H. Lee, Y.Y. Jeong, S. Jon,Antibiofouling polymer-coated gold nanoparticles as a contrast agent for in vivo X-ray computed tomography imaging (vol 129, pg 7661, 2007), J Am Chem Soc, 129 (2007) 12585-12585.

[33] S.C. Barnett, A.J. Roskams,Olfactory ensheathing cells: isolation and culture from the neonatal olfactory bulb, Methods Mol Biol, 438 (2008) 85-94.

[34] L.M. Lacroix, N.F. Huls, D. Ho, X.L. Sun, K. Cheng, S.H. Sun,Stable Single-Crystalline Body Centered Cubic Fe Nanoparticles, Nano Lett, 11 (2011) 1641-1645.

[35] S. Peng, Sun, S.,Synthesis and characterization of monodisperse hollow Fe3O 4 nanoparticles, Angewandte Chemie - International Edition 46 (2007) 4155-4158

[36] S. Volden, Kjøniksen, A.-L., Zhu, K., Genzer, J., Nyström, B., Glomm, W.R,Temperature-Dependent Optical Properties of Gold Nanoparticles Coated with a Charged Diblock Copolymer and an Uncharged Triblock Copolymer, Acs Nano, 4 (2010) 1187-1201.

[37] G. Singh, P.A. Kumar, C. Lundgren, A.T.J. van Helvoort, R. Mathieu, E. Wahlström, W.R. Glomm,Tunability in Crystallinity and Magnetic Properties of Core–Shell Fe Nanoparticles, Part Part Syst Char, (2014).

[38] X.Q. Li, W.X. Zhang,Sequestration of metal cations with zerovalent iron nanoparticles - A study with high resolution X-ray photoelectron spectroscopy (HR-XPS), Journal of Physical Chemistry C, 111 (2007) 6939-6946.

[39] P.E. Jonsson,Superparamagnetism and Spin Glass Dynamics of Interacting Magnetic Nanoparticle Systems, Adv Chem Phys, 128 (2004) 191-248.

[40] W.D. Callister, Materials Science and Engineering:An Introduction, John Wiley & Sons, Inc, 2007.

[41] G.F. Goya, T.S. Berquo, F.C. Fonseca, M.P. Morales,Static and dynamic magnetic properties of spherical magnetite nanoparticles, J Appl Phys, 94 (2003) 3520-3528.

[42] H. Khurshid, C.G. Hadjipanayis, H.W. Chen, W.F. Li, H. Mao, R. Machaidze, V. Tzitzios, G.C. Hadjipanayis,Core/shell structured iron/iron-oxide nanoparticles as excellent MRI contrast enhancement agents, J Magn Magn Mater, 331 (2013) 17-20.

[43] A. Figuerola, R. Di Corato, L. Manna, T. Pellegrino,From iron oxide nanoparticles towards advanced iron-based inorganic materials designed for biomedical applications, Pharmacol Res, 62 (2010) 126-143.

[44] I. Sandvig, L. Hoang, T.C.P. Sardella, S.C. Barnett, C. Brekken, K. Tvedt, M. Berry, O. Haraldseth, A. Sandvig, M. Thuen,Labelling of olfactory ensheathing cells with micron-sized particles of iron oxide and detection by MRI, Contrast Media Mol I, 7 (2012) 403-410.

[45] I. Sandvig, M. Thuen, L. Hoang, O. Olsen, T.C.P. Sardella, C. Brekken, K.E. Tvedt, S.C. Barnett, O. Haraldseth, M. Berry, A. Sandvig,In vivo MRI of olfactory ensheathing cell grafts and regenerating axons in transplant mediated repair of the adult rat optic nerve, Nmr Biomed, 25 (2012) 620-631.

[46] E. Bible, O. Qutachi, D.Y.S. Chau, M.R. Alexander, K.M. Shakesheff, M. Modo,Neo-vascularization of the stroke cavity by implantation of human neural stem cells on VEGF-releasing PLGA microparticles, Biomaterials, 33 (2012) 7435-+.

1.7 Figures

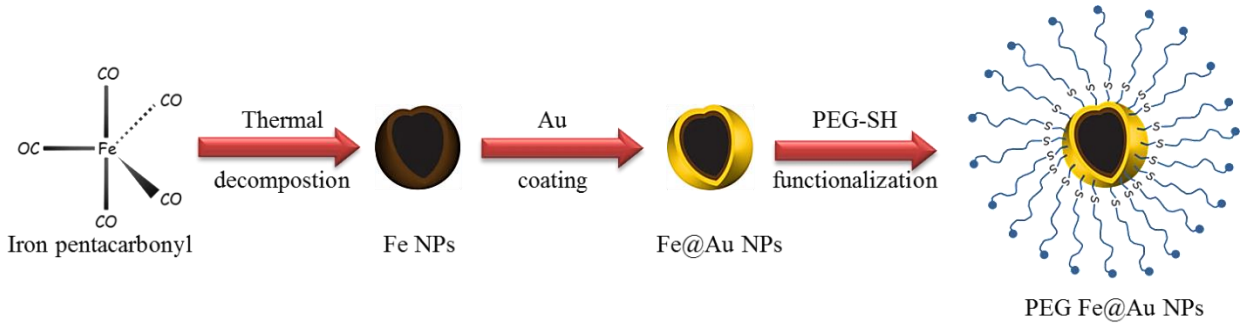

Figure 1 Simplified schematic showing sequence of synthesis of PEG modified Fe@Au NPs.

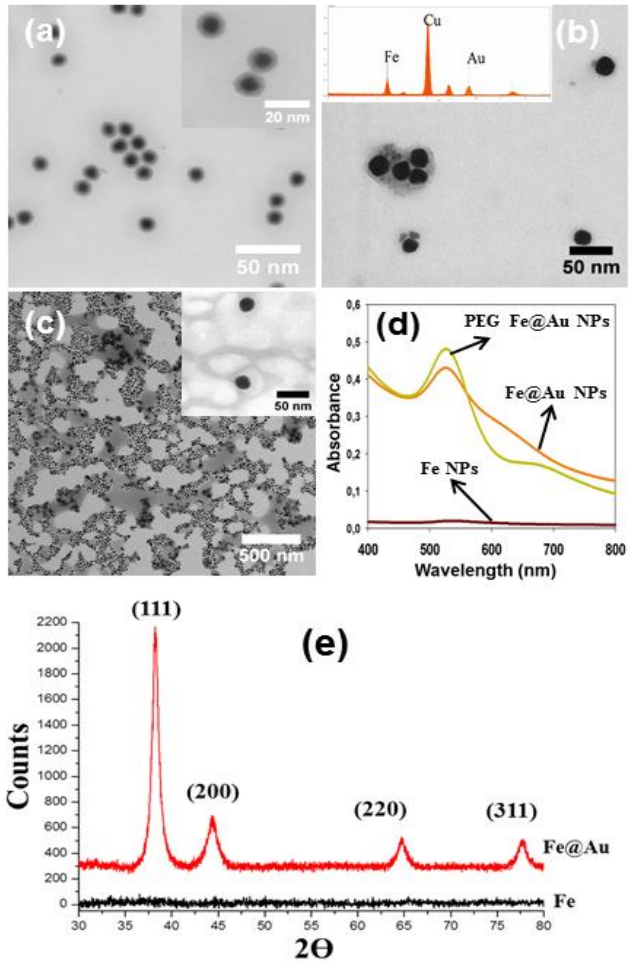

Figure 2 Representative BF S(T)EM images of (a) $Fe@Fe_xO_y$ NPs (inset is an magnified image of Fe NPs) ,(b) Fe@Au NPs (inset is EDX spectrum for Fe@Au NPs), (c) PEG functionalized

Fe@Au NPs (enlarged view of PEG functionalized Fe@Au NPs). (d) UV-Vis spectra of Fe,Fe@Au and PEG Fe@Au NPs. (e) XRD spectra for Fe and Fe@Au NPs.

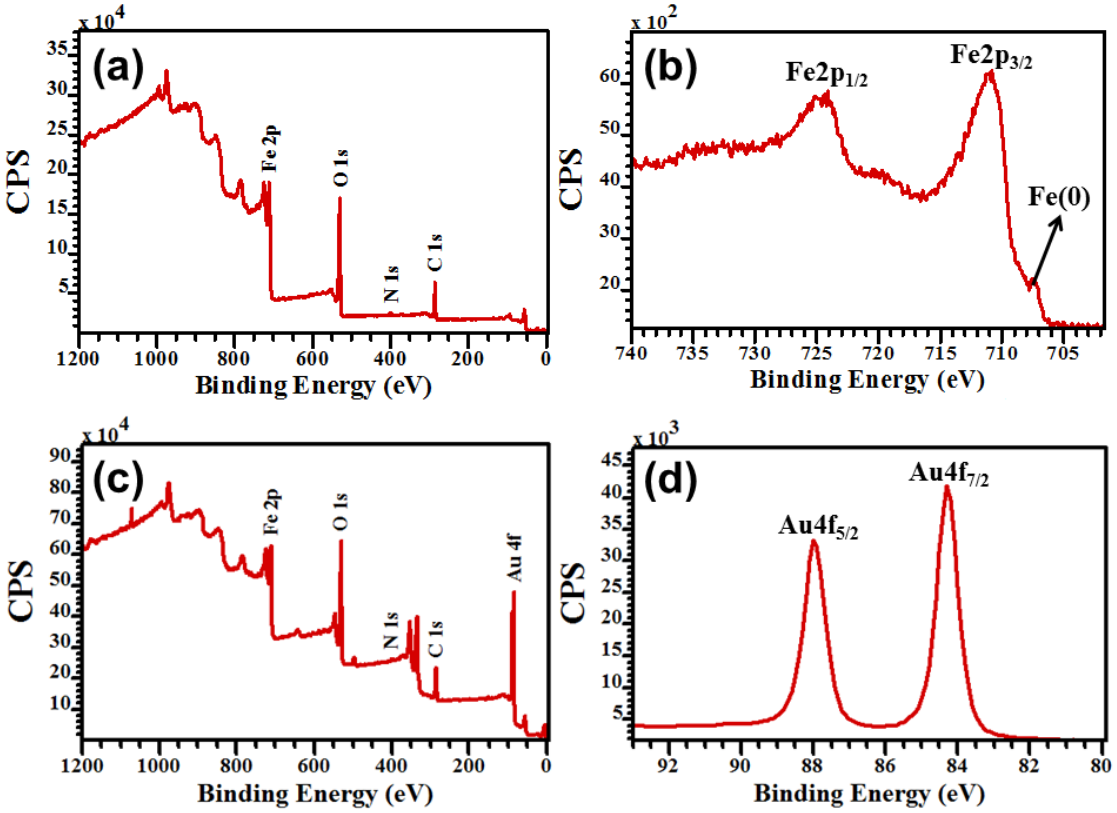

Figure 3 (a) XPS survey spectra of Fe-NPs (b) High resolution narrow region scan of Fe2p (b) XPS survey spectra of Fe@Au NPs (d) High resolution narrow region scan of Au4f.

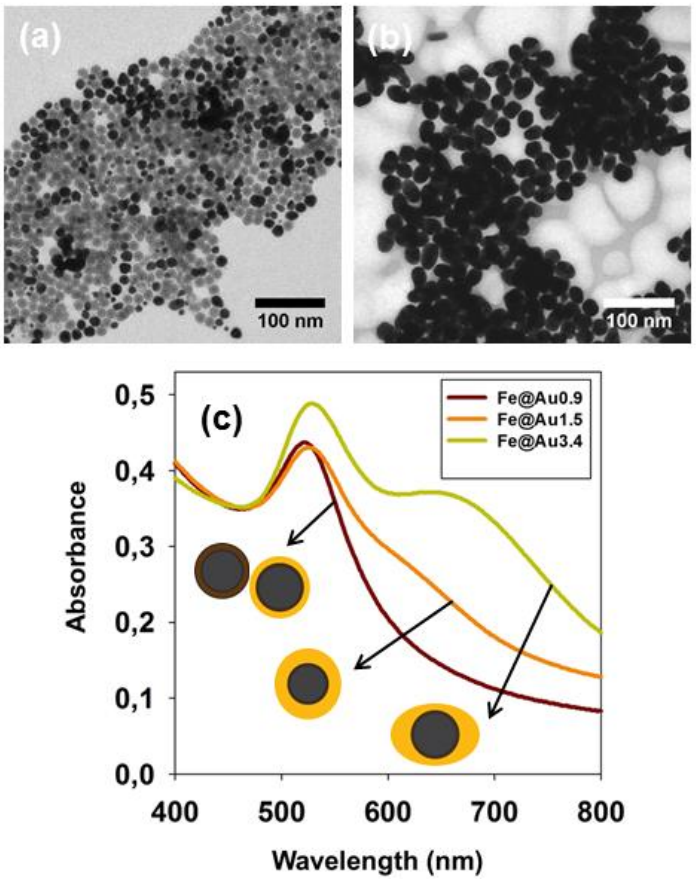

Figure 4 BF S(T)EM images showing Fe@Au NPs formation at different Au precursor concentration, (a) 0.9 mM, (b) 3.4 mM. (c) UV-Vis spectra of Fe@Au NPs synthesized using different concentrations of Chloroauric acid 0.9 mM, 1.5 mM and 3.4 mM.

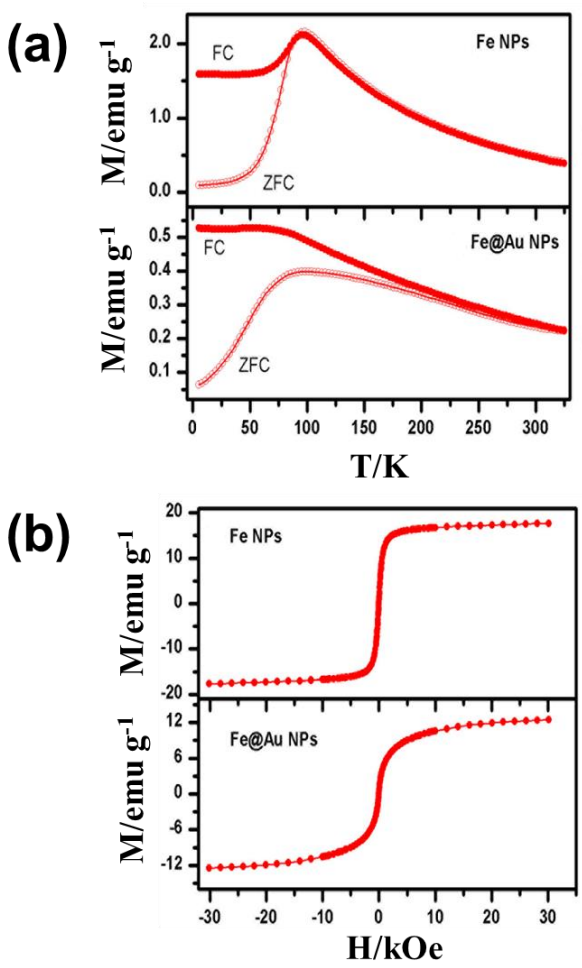

Figure 5(a) Temperature dependence of ZFC and FC magnetization curves measured in 20 Oe field for Fe and Fe@Au NPs (c) Magnetic hysteresis curves at 300K for Fe and Fe@Au NPs.

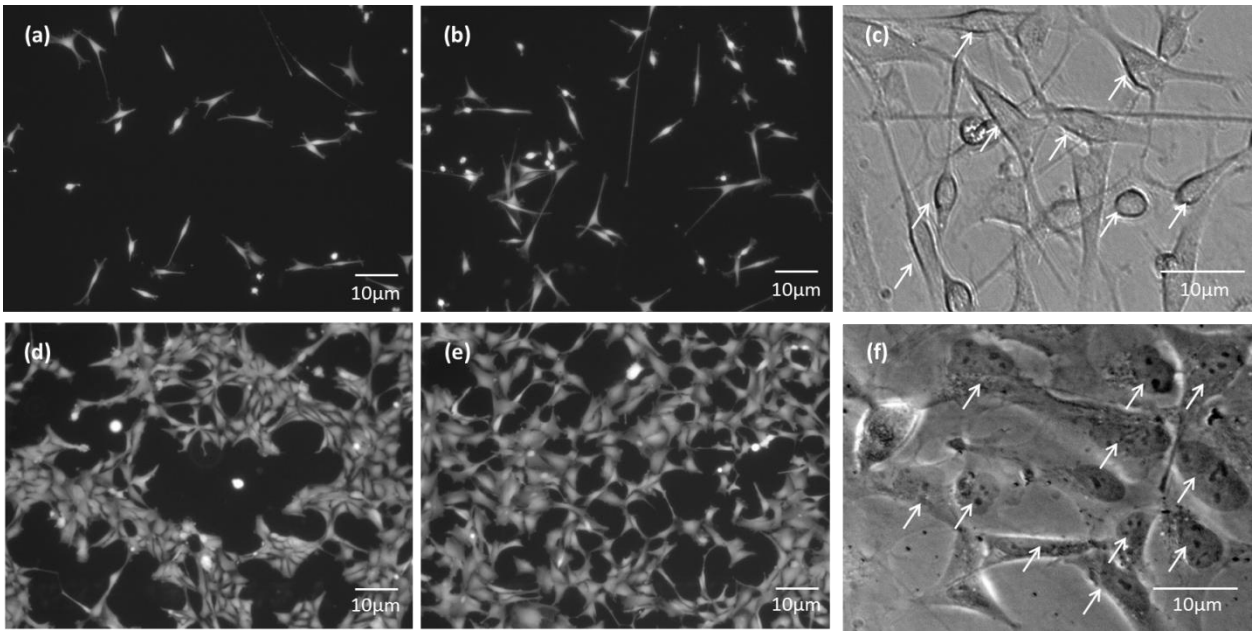

Figure 6 (a),(b),(d),(e) Live/Dead images of OECs and NSCs 24h after labeling with Fe@Au NPs (a) Unlabelled OECs (b) OECs with Fe@Au NPs (d) Unlabelled NSCs (e) NSCs with Fe@Au NPs (c),(f) DIC images of labeled OECs and NSCs, respectively, showing Fe@Au uptake (arrows).

Supporting Information

Synthesis and *in vitro* cellular interactions of superparamagnetic iron nanoparticles with a crystalline gold shell

Sulalit Bandyopadhyay[1*], *Gurvinder Singh*[1], *Ioanna Sandvig*[2], *Axel Sandvig*[2,3], *Roland Mathieu*[4], *P. Anil Kumar*[4], *Wilhelm Robert Glomm*[1,5]

[1]Ugelstad Laboratory, Department of Chemical Engineering,

[2] MI Lab and Department of Circulation and Medical Imaging,

Norwegian University of Science and Technology (NTNU), N-7491 Trondheim, Norway.

[3] Department of Neurosurgery, Umeå University Hospital, Umeå, Sweden.

[4]Department of Engineering Sciences, Uppsala University, Box 534, SE-75121, Uppsala, Sweden.

[5]Sector of Biotechnology and Nanomedicine, SINTEF Materials and Chemistry, N-7465, Trondheim, Norway.

[*]Corresponding author's email address: sulalit.bandyopadhyay@ntnu.no

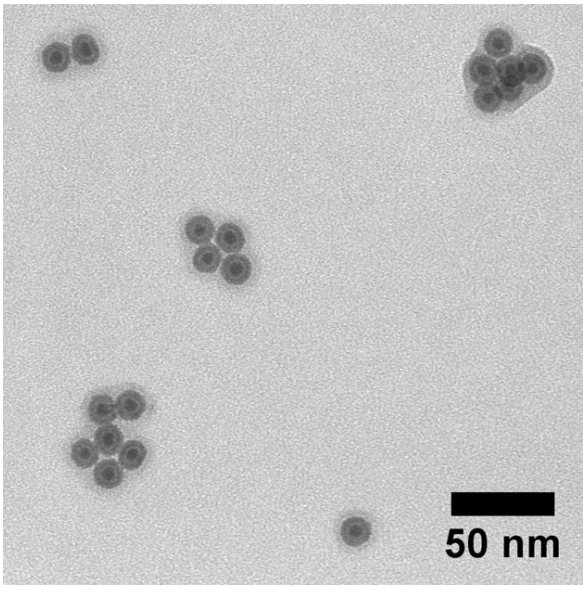

Figure S1 BF S(T)EM image of citrate stabilized Fe NPs in an aqueous phase

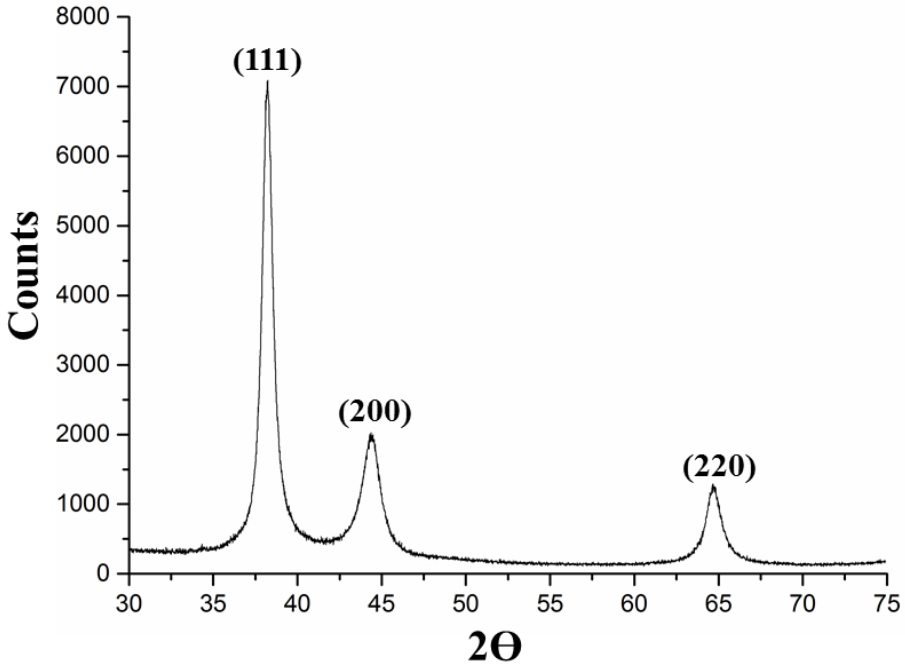

Figure S2 XRD pattern of Fe@Au NPs synthesized at high concentration of gold precursor (3.4 mM).

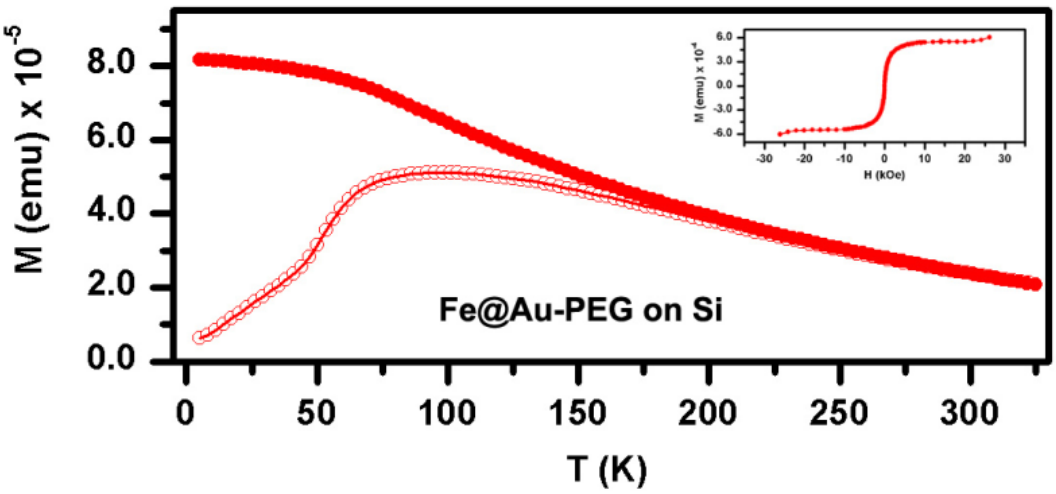

Figure S3 Magnetization hysteresis curves of Fe@Au-PEG deposited on Si. The FC magnetization curves continue to increase until the lowest temperature measured, signifying further weakening of inter particle interactions on addition of PEG molecules. The inset shows the magnetic hysteresis loop measured at 300 K for the same sample.